Directional lasing in resonant semiconductor nanoantenna arrays

Son Tung Ha[1,2,5], Yuan Hsing Fu[1,3,5], Naresh Kumar Emani [1,4,5], Zhenying Pan[1,2], Reuben M. Bakker[1,2], Ramón Paniagua-Domínguez [1,2] and Arseniy I. Kuznetsov[1,2]*

High-index dielectric and semiconductor nanoparticles supporting strong electric and magnetic resonances have drawn significant attention in recent years. However, until now, there have been no experimental reports of lasing action from such nanostructures. Here, we demonstrate directional lasing, with a low threshold and high quality factor, in active dielectric nanoantenna arrays achieved through a leaky resonance excited in coupled gallium arsenide (GaAs) nanopillars. The leaky resonance is formed by partially breaking a bound state in the continuum generated by the collective, vertical electric dipole resonances excited in the nanopillars for subdiffractive arrays. We control the directionality of the emitted light while maintaining a high quality factor ($Q = 2,750$). The lasing directivity and wavelength can be tuned via the nanoantenna array geometry and by modifying the gain spectrum of GaAs with temperature. The obtained results provide guidelines for achieving surface-emitting laser devices based on active dielectric nanoantennas that are compact and highly transparent.

Dielectric nanoantennas with low dissipative losses at visible and near-infrared wavelengths provide a more promising way to efficiently manipulate light at the nanoscale compared with conventional plasmonics[1–4]. Another advantage of many suitable dielectric materials is their compatibility with semiconductor fabrication processes, which is promising for on-chip integration in photonic devices. Finally, the wealth of optical modes accessible in dielectric nanoparticles—even in their simplest shapes—and their associated interference effects bring exciting opportunities to realize optical antennas with strong directionality that are straightforward to fabricate. Due to these advantages, many applications of resonant dielectric nanostructures have been proposed and demonstrated in the past few years, such as beam bending and switching[5–10], flat lenses[11–14], nonlinear harmonic generation[15–18], directional scattering[19–21], hologram and vortex-beam generation[6,7,22–24], and polarization control[24,25].

A particularly important characteristic of any photonic system is the ability to produce amplified spontaneous or stimulated emission. While dielectric resonant nanostructures have been studied for light confinement and enhanced spectroscopies (Raman and fluorescence[26–29]), up to now, despite some theoretical proposals[30], there has been no experimental demonstration of lasing action based on dielectric nanoantenna concepts. The main reasons can be attributed to the low quality factor (Q) of the resonant modes and, thus, the lack of suitable cavity designs.

Recently, a novel method of light confinement has been demonstrated by means of so-called bound states in the continuum (BICs). In these states, light is localized within the structure supporting the BIC mode, despite the mode lying in the continuum part of the spectrum, therefore coexisting with the radiative modes[31–34]. Theoretically, the Q factor of these modes can reach infinity if the BIC condition is strictly satisfied[33]. In practice, the Q factor is limited by the finite size of real systems, which implies the existence of unprotected channels and renders the BIC into so-called supercavities

or leaky resonances[33,35–37] (leaky resonances may emerge even for infinite systems[37]). Nevertheless, the high Q values achievable even in real, practical systems supporting these modes make them perfectly suitable for lasing, and some devices working under this principle have recently been described[38–42]. A common limitation of these devices is the poor directionality of the emitted light, which is radiated into free space by defects or simply by the edges of the device[43].

Here, we propose a design that takes advantage of both dielectric nanoantenna resonances and BIC confinement to experimentally realize lasing in a two-dimensional (2D) array of resonant dielectric nanostructures with controlled directionality.

Lasing cavity based on a BIC

The BIC is formed at the gamma (Γ) point of the array; that is, for the emission wave-vector $\mathbf{k}_{||} = (k_x, k_y) = 0$, where k_x and k_y are the components of the wave-vector along the x and y directions, when the particles support only the resonant vertical dipole mode (that is, oriented along the z axis, normal to the array) and the array is strictly subdiffractive and of infinite size in the x and y directions (see Fig. 1a,b). In this situation, it is easy to visualize how the BIC is formed. For a subdiffractive, 2D array of dipoles oscillating in phase, radiation is only allowed in the normal direction to the array (in all other directions, destructive interference from the rest of the dipoles in the array leads to zero net radiation). In the case in which these dipoles oscillate precisely in the normal direction, and therefore do not radiate towards it, no radiation from the system is allowed, and the BIC is formed. This BIC is topologically robust. The polarization vector forms a vortex around the $k_x = k_y = 0$ point with topological charge $q = 1$ (and nodal lines $E_x = 0$ along $k_x = 0$ and $E_y = 0$ along $k_y = 0$), and therefore cannot be removed unless strong variations in the geometric parameters of the system are introduced[44]. Now, by carefully adjusting one of the periods to support a diffraction order at the resonant wavelength, a leaky channel can

[1]Data Storage Institute, Agency for Science, Technology and Research, Singapore, Singapore. [2]Present address: Institute of Materials Research and Engineering, Agency for Science, Technology and Research, Singapore, Singapore. [3]Present address: Institute of Microelectronics, Agency for Science, Technology and Research, Singapore, Singapore. [4]Present address: Indian Institute of Technology, Hyderabad, India. [5]These authors contributed equally: Son Tung Ha, Yuan Hsing Fu, Naresh Kumar Emani. *e-mail: arseniy_kuznetsov@imre.a-star.edu.sg
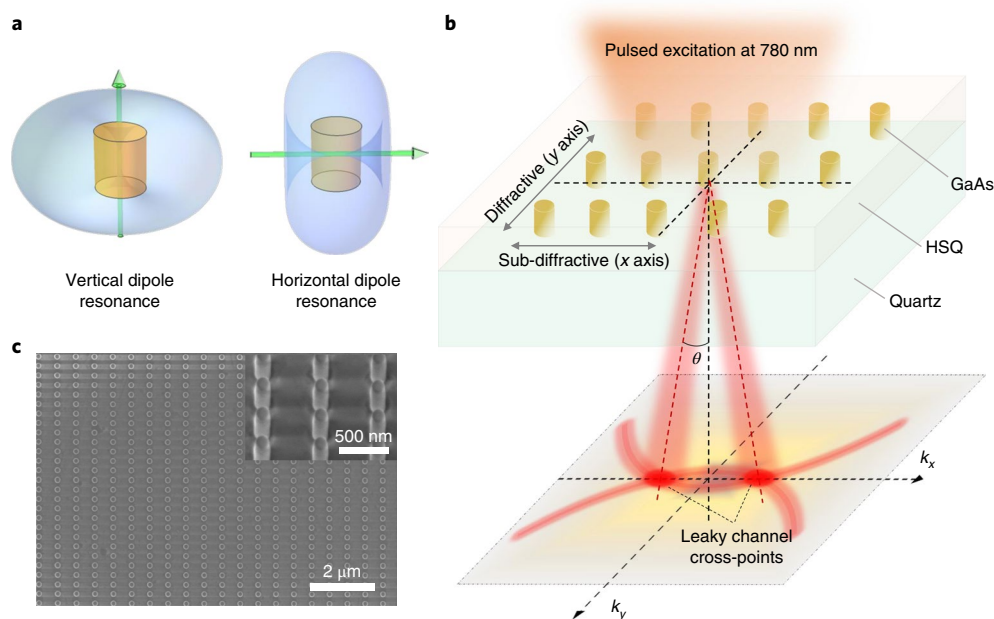
Fig. 1 | Structure of the resonant dielectric nanoantenna array. a, Resonant modes in a dielectric nanopillar showing the vertical and horizontal dipole resonances. The GaAs pillar in our laser device has a diameter of 100 nm and a height of 250 nm. **b**, Schematics of the GaAs nanopillar array on a fused silica substrate embedded in hydrogen silsesquioxane (HSQ) resist (spin-on glass). Along the y axis, the period ($P_y = 540$ nm) is designed to support diffraction at the emission wavelength range of GaAs (~830 nm at 77 K). Along the x axis, the period is fixed at 300 nm and is subdiffractive. **c**, SEM image of the fabricated array at normal incidence. Inset: SEM image at a 30° tilted angle, showing the cylinder shape.

be opened[37]. In this way, it is possible to control the directionality of the emission while still maintaining a very high confinement factor of the cavity near the vertical direction. This design can be applied to various active high-index semiconductor materials to achieve lasing at visible and infrared wavelengths. Moreover, the low surface footprint of our laser structure leads to high transparency in the wavelength range of interest (for example, >85% over 750–900 nm). This surface-emitting laser might have applications in multi-layered photonic devices.

Our laser device consists of vertical coupled gallium arsenide (GaAs) nanopillars as building blocks with a diameter of ~100 nm and a height of 250 nm. GaAs is a widely used III–V semiconductor with a near-infrared direct bandgap at ~1.42 eV (300 K) and a relatively high refractive index of ~3.5 (refs [45,46]). Recently, GaAs-based metasurfaces have also been studied for second-harmonic generation and optical modulation[16,47,48]. When using GaAs, it should be noted that it presents a high surface-charge recombination due to defects at room temperature, which becomes especially important in nanoscaled samples[49]. This leads to a poor external quantum efficiency of the material photoluminescence. In our sample, neither a surface passivation layer (for example, AlGaAs) nor a chemical treatment process was applied. To increase the emission yield, we performed the measurements at low temperature (that is, 77 K), and thus the emission wavelength of GaAs was blue-shifted to ~830 nm from the usual room temperature peak at ~870 nm. Hence, we will discuss our design concept based on the emission of GaAs at this particular wavelength (that is, 830 nm). In our device, both vertical and in-plane dipole resonances are supported in the nanopillars, as illustrated in Fig. 1a. The nanopillars are arranged in a 2D rectangular array, supported by a quartz substrate and embedded in silica (SiO₂), as depicted in Fig. 1b. In one of the directions, the period of the lattice is subdiffractive for wavelengths within the photoluminescence band of GaAs (namely, the x axis; $P_x = 300$ nm), while in the other direction, the period is diffractive (namely, the y axis; $P_y = 540$ nm). This design opens up a radiation channel that turns

the BIC mode of the purely subdiffractive case into a leaky resonance with finite Q (see further details in Supplementary Figs. 1 and 2) and presents a cross-point with $k_y = 0$ in the emission plane, as schematically depicted in Fig. 1b.

GaAs nanopillar arrays were fabricated on a fused silica substrate using epitaxial lift-off of a GaAs film, e-beam lithography and dry etching techniques, and embedded into a homogeneous medium with a refractive index of ~1.5, as described in detail in Supplementary Fig. 3. The scanning electron microscope (SEM) images of one of the fabricated GaAs arrays before final coating are shown in Fig. 1c. To investigate the resonant modes in the GaAs array, we performed spectrally resolved back focal plane imaging[14] (see Methods). The schematic of the measurement set-up is illustrated in Fig. 2a.

Figure 2b shows the measured transmission for p-polarized light (polarization along the x axis at normal incidence) passing through the GaAs nanopillar array as a function of the wavelength and the angle of incidence. The results show two resonant bands in the system (manifested as dips in transmission). The lowest energy band narrows and then vanishes when incidence becomes normal. The transmission spectra at various angles, as extracted from Fig. 2b, are shown in Supplementary Fig. 4. The resonance at ~825 nm vanishes at 0° while the other mode at ~790 nm is red-shifted for decreasing angle of incidence. To understand the nature of these resonant modes, we performed numerical simulations of the transmission spectrum dependence on angular incidence using a commercial electromagnetic solver based on the finite element method (COMSOL Multiphysics). The results, presented in Fig. 2c, are in a very good agreement with the experimental ones, showing two resonance modes at ~790 and ~825 nm for close-to-normal incidence that blue-shift as the angle increases. Multipole decomposition of the displacement currents induced in the nanopillars is used to identify the nature of these resonances. The results of this analysis are plotted in Fig. 2d. They clearly show that the resonant dips observed in the transmission spectra correspond to a diffractively coupled,
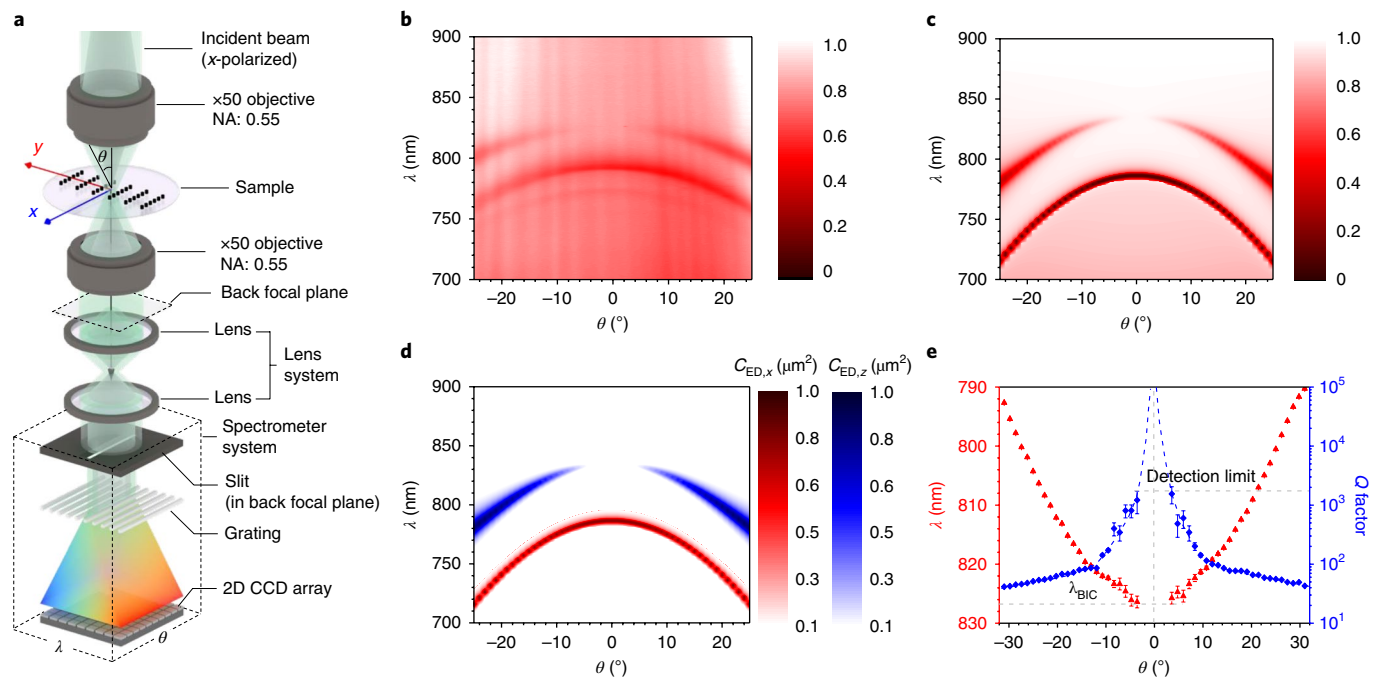
Fig. 2 | Resonant modes in the GaAs nanopillar array. a, Schematic of the spectrally resolved back focal plane imaging measurements. CCD, charge-coupled device. **b**, Angular-resolved transmission spectrum image measured for an array consisting of GaAs nanopillars with 100 nm diameter, 250 nm height and a 540 nm period along the y axis. The period along the x axis is 300 nm. The measured data correspond to a varying angle of incidence contained in the x–z plane of the sample and p-polarization. **c**, Simulated transmission as a function of the angle and wavelength of incidence. **d**, Numerically calculated multipolar decomposition, showing the two modes excited in the nanopillars as a function of the angle and wavelength of incidence. In particular, the colour maps represent the scattering cross section associated with a horizontal electric dipole (red colour scale, $C_{ED,x}$) and a vertical electric dipole (blue colour scale, $C_{ED,z}$). The simulations show that the resonance dip observed in transmission at ~830 nm for oblique incidence corresponds to the excitation of a vertical electric dipole resonance, which vanishes at 0° forming the BIC. **e**, Angular dependence of the wavelength and Q factor for the vertical electric dipole mode extracted from **b** showing emergence of the BIC with Q factor growing to infinity at λ_{BIC} ~ 830 nm. The resonance wavelength shifts to higher energy and the Q factor decreases when the angle increases. The error bar in the Q factor plot originates from the uncertainty in the peak fitting to determine FWHM.

x-oriented, in-plane electric dipole and a z-oriented vertical electric dipole, for the high- and low-energy resonances, respectively. Details of both the numerical simulations and the multipole decomposition can be found in the Methods. The resonance at 825 nm is associated with the vertical dipole vanishing at normal incidence, corresponding to the emergence of the symmetry-protected, leaky resonance associated with the bound state at the Γ point of the first Brillouin zone for the purely subdiffractive array. Figure 2e shows the angle-dependent wavelength and Q factor of the vertical electric dipole resonance extracted from angle-resolved transmission data in Fig. 2b. As can be seen, the Q factor sharply increases as the angle decreases below 10°. The Q factor reaches ~1,500 at around 4°, which is at the resolution limit of the spectrometer (~0.6 nm for 150 g mm⁻¹ grating). This behaviour confirms the BIC characteristic of the resonant mode.

Directional lasing in the 2D GaAs nanopillar array

To demonstrate lasing, the 2D GaAs nanopillar array was placed in a liquid nitrogen-cooled cryostat (ST-500; Janis Research) and optically pumped using a femtosecond laser (780 nm, 200 fs pulse width at a repetition rate of 100 KHz). The pumping laser was focused on the sample using a ×5 microscope objective resulting in a laser spot diameter of ~40 μm. The emission signal from the array was collected using a ×50 long working distance microscope objective (NA = 0.45) and dispersed in the spectrometer using a 1,200 g mm⁻¹ grating with 1,000 nm blaze giving a spectral resolution of 0.1 nm. A long pass filter (800 nm; Thorlabs) was used to filter out the excitation laser line.

Figure 3a shows the normalized evolution of the emission spectra of the nanopillar array when pumping it at different laser fluences. The top panel in Fig. 3b shows the output intensity in log–log scale of the photoluminescence as a function of the pumping fluence. The observed S shape represents the spontaneous emission to amplified spontaneous emission to stimulated emission transition with a threshold of ~14 μJ cm⁻², which is conventionally defined by the kink in the log–log curve. When the pumping fluence is above 10 μJ cm⁻², a high-intensity, narrow peak appears at ~825 nm. The full width at half maximum (FWHM) of the photoluminescence also decreases from 8 nm to a minimum of ~0.3 nm, corresponding to a lasing Q factor of 2,750. Here, the Q factor of the laser emission is defined by the emission wavelength divided by its FWHM. To further verify that the emission of our device indeed corresponds to lasing, we measured the second-order photon correlation function using a Hanbury–Brown–Twiss set-up[50] (see details in Supplementary Fig. 5). The normalized intensity correlation at zero time delay g²(0) as a function of pumping fluence is shown in the bottom panel of Fig. 3b. The result shows that g²(0) reaches unity when the pumping fluence is above 20 μJ cm⁻², indicating a coherent light emission. It is noted that the g²(0) value decays at a pumping fluence lower than ~15 μJ cm⁻² instead of approaching the theoretical value g²(0) = 2 for an ideal thermal light source. This happens because the coherence time drops below the detection limit of our set-up (that is, 81 ps). A similar observation has been reported and thoroughly discussed previously[51]. Figure 3c shows the optical image (top) and the photoluminescence images below (middle) and above (bottom) the lasing threshold. The red dashed
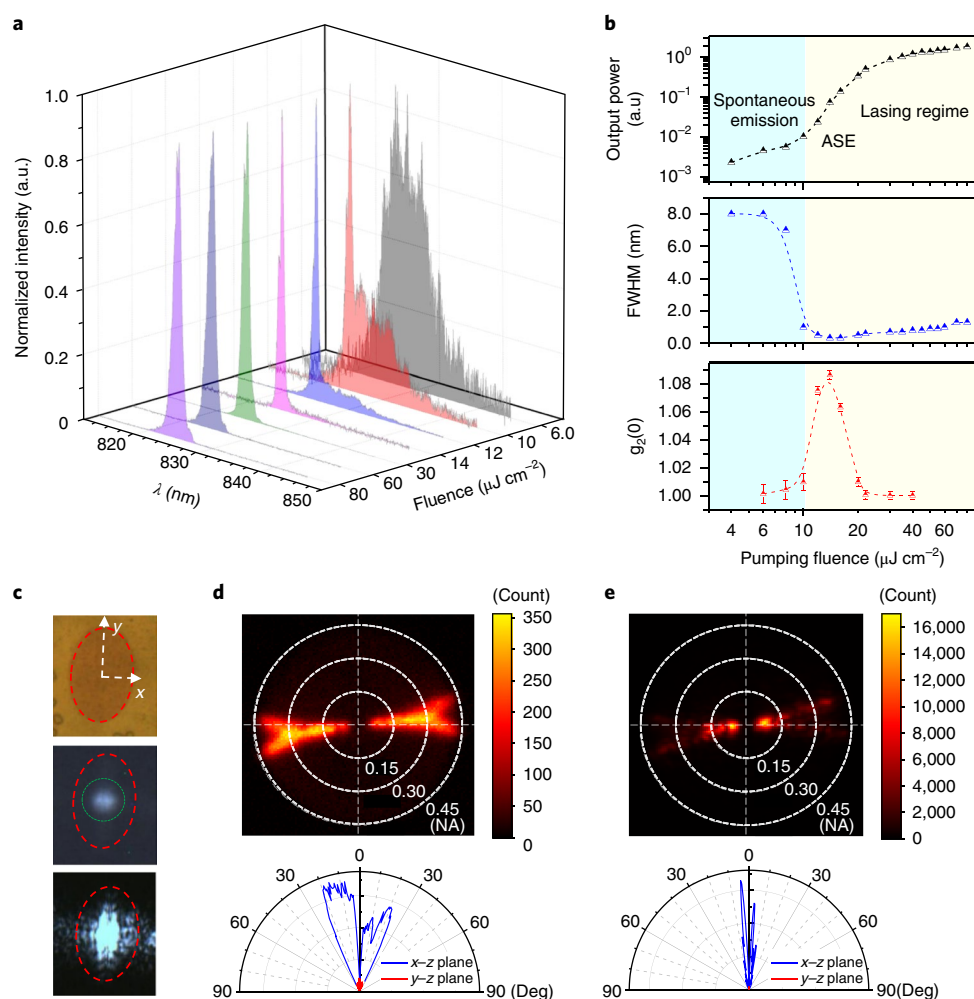
Fig. 3 | Lasing action in the resonant semiconductor nanoantenna array. a, Evolution of the normalized emission spectra of the GaAs nanopillar array at different pumping fluences. **b**, Top, integrated output intensity of the emission peak as a function of input fluence in log–log scale. The observed S curve (black dashed line) in the input–output dependence shows the transition from spontaneous to amplified spontaneous and then to stimulated emission. ASE, amplified spontaneous emission. Middle, FWHM of the emission peak at different pumping fluences. Bottom, evolution of the second-order emission intensity correlation function at zero time delay $g^2(0)$ at different pumping fluences. Above a pumping fluence of $20\,\mu\mathrm{J\,cm^{-2}}$, $g^2(0)$ approaches unity, confirming that coherent lasing has been achieved. The error bar of $g^2(0)$ originates from variations of the correlation function intensity for neighbouring pulses. **c**, Top, optical image taken under white light illumination showing the edge of the GaAs array (red dashed oval) and defined x and y axes along the rectangular lattice. The middle and bottom panels show fluorescence images under femtosecond laser excitation below and above the lasing threshold, respectively. The green dashed circle in the middle panel shows the pumping laser spot. The fluorescence image was collected using a charge-coupled device camera with an 820 nm band-pass filter (FWHM = 20 nm) to cut out the excitation laser line. The exposure time in the middle image is 20× higher than that of the bottom one to clearly show the spontaneous emission. **d,e**, Back focal plane image (top) and directivity (bottom) of the emission below (**d**) and above (**e**) the lasing threshold, collected by a long working distance 50× microscope objective (NA = 0.45). The directivity plots were obtained as cuts along the x and y axes from the back focal plane images.

oval in these images corresponds to the array size, with the x and y axis labelled. The green dashed circle in the middle image represents the pumping laser spot, which is about 40 μm in diameter. To determine the lasing directivity, the back focal plane images of the emission are collected using a long working distance ×50 microscope objective (NA = 0.45). The images and extracted directivity of the emission below and above the lasing threshold are shown in Fig. 3d,e, respectively. Below the threshold, the emission directivity follows two photonic bands due to the grating effect of the diffraction periodicity along the y axis. In contrast, above the threshold, the lasing emission only happens at a specific angle (that is, ~3° to the normal axis) along the x axis. This angle corresponds to the crossing point of the emission bands, with k_x in the emission plane (leaky channel cross points). Polarization dependence measurement of the

emission intensity also shows maximum values along the x axis (as shown in Supplementary Fig. 6).

In general, the lasing threshold is inversely proportional to the optical gain (g) and the confinement factor (Γ_E): $P_\mathrm{th} \sim (g(\lambda) \times \Gamma_\mathrm{E})^{-1}$. As discussed in Fig. 2, as the angle of incidence (or, by reciprocity, the angle of emission), θ, approaches 0, the resonance wavelength is red-shifted and the Q factor dramatically increases (Γ_E increases). Thus, the lasing happens at the wavelength and angle where the minimum lasing threshold is achieved. It should be noted that the emission bands below the lasing threshold, shown in Fig. 3d, vanish near the normal axis. This is due to the fact that the emission is a combination of the lattice effect (emission along the diffraction directions) and the emission of vertical dipoles, which resonantly enhance the photoluminescence and which have vanishing
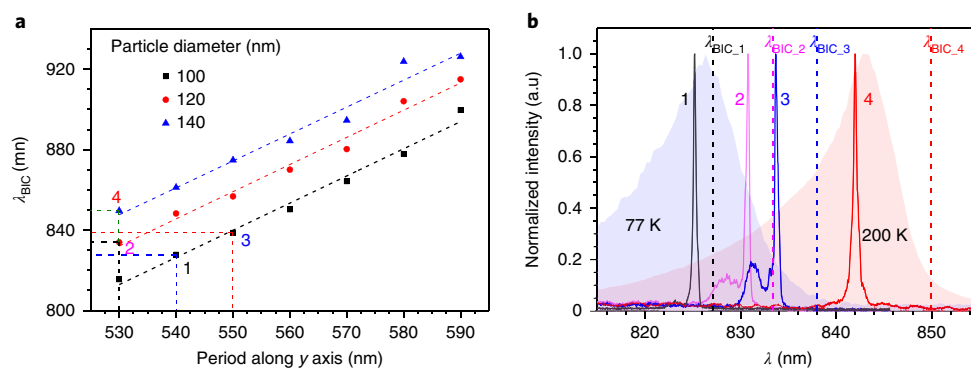
Fig. 4 | Wavelength-tunable lasing in dielectric nanoantenna array. a, Resonance wavelength under the quasi-BIC condition for arrays with different geometric parameters (nanopillar diameter and array period along the y axis). The coloured numbers correspond to the arrays chosen for lasing measurement in **b**. **b**, Lasing spectra for arrays 1–4 with parameters as indicated in **a**. Lasing measurements were performed at 77 K for arrays 1–3 and 200 K for array 4. This was done to match the gain spectrum of GaAs with the designed resonance wavelength of the selected arrays, as shown by the photoluminescence spectra of GaAs for different temperatures plotted as shaded areas.

emission at angles close to the normal direction (the oscillation direction of the dipoles). The resonantly enhanced photoluminescence is discussed in more detail in Supplementary Fig. 7. Another interesting feature of the system is that, when higher pumping fluence is used, higher energy modes are also excited, with lower Q and a higher emission angle (see Supplementary Fig. 8). By changing the temperature of the device, it is possible to spectrally move the maximum of the gain in such a way that the minimum threshold happens at higher angles, despite having a lower Q factor. In this way, it is possible to obtain directional lasing at an angle as large as ~25° (see Supplementary Fig. 9).

Lasing wavelength tunability
One of the advantages of using the vertical dipole resonance mode in our laser structure is that the leaky resonance from the BIC condition can be satisfied with a wide range of geometric parameters. By tuning either the particle diameter or the y axis period, the quasi-BIC resonant wavelength can be precisely tuned. Figure 4a shows the leaky resonance wavelength for various arrays with different particle sizes and periods, extracted from angle-resolved transmission measurements (see Supplementary Fig. 10 for full data). Also, by changing the temperature from 77–200 K, the peak of the gain spectrum of GaAs can be shifted from 830–850 nm (see Supplementary Fig. 11). Combining these two effects, it is possible to achieve lasing at different selected angles and wavelengths from different resonant arrays. Figure 4b shows lasing spectra achieved for 4 different arrays (corresponding to the same colour-dashed circles in Fig. 4a) at 77 K (for arrays 1–3) and 200 K (for array 4). Attempts to achieve lasing at a higher temperature were not successful because of the low gain of GaAs caused by its high surface recombination. We believe that by using higher gain material or improving the emission quantum efficiency of GaAs (for example, by surface passivation) it should become possible to achieve lasing at room temperature.

Conclusion
We have experimentally demonstrated directional lasing action in arrays of active dielectric nanoantennas. This was achieved using vertical electric dipole resonances excited inside GaAs nanopillars, which, in the purely non-diffractive case, would form a non-radiative BIC. The directionality of the laser was controlled by a leaky channel, opened by designing one period of the array to support diffractive orders. The lasing happened at the angle where the emission bands (defined by the leaky channel) presented a crossing point in the emission plane. Despite the presence of the radiation channel, sufficiently high Q factors could be retained for small lasing angles (that is, <10°).

Moreover, lasing could also be obtained at an angle as large as 25° to the normal. This was achieved by temperature-induced tuning of the gain spectrum to compensate for the lower Q factor corresponding to a larger angle, and led to a minimum lasing threshold at the corresponding wavelength. By tuning geometric parameters of the array, such as particle size or period, the leaky resonance wavelength could be precisely controlled to achieve lasing at different wavelengths. This design concept can be applied to other high-index active semiconductor materials and can be readily integrated in multi-layered photonic devices due to its high transparency. Magnetic dipole and higher-order multipole resonances can also be used to generate BIC modes in this scheme, provided the symmetry protection is preserved[33]. Our results demonstrate that Mie resonances in dielectric nanoparticles can be used to achieve stimulated emission even in relatively low-gain materials such as unpassivated GaAs. While the array sizes used in our experiments were chosen to be large enough as to closely mimic an infinite system (namely, on the order of 200 × 200 particles), recent studies suggest that quasi-BIC modes sustaining large Q factors can be achieved for systems with as few as 8 × 8 unit cells in 2D arrays[42] and 5 of them in one directional ones[52], opening pathways to further miniaturization of these devices. This brings new opportunities to nanophotonic research by providing a platform for making highly efficient directional emitting devices based on active semiconductor nanoantennas.

Methods
Methods, including statements of data availability and any associated accession codes and references, are available at https://doi.org/10.1038/s41565-018-0245-5.

References
1. Kuznetsov, A. I., Miroshnichenko, A. E., Brongersma, M. L., Kivshar, Y. S. & Luk'yanchuk, B. Optically resonant dielectric nanostructures. *Science* **354**, aag2472 (2016).
2. Staude, I. & Schilling, J. Metamaterial-inspired silicon nanophotonics. *Nat. Photon.* **11**, 274–284 (2017).
3. Kuznetsov, A. I., Miroshnichenko, A. E., Fu, Y. H., Zhang, J. & Luk'yanchuk, B. Magnetic light. *Sci. Rep.* **2**, 492 (2012).
4. Evlyukhin, A. B. et al. Demonstration of magnetic dipole resonances of dielectric nanospheres in the visible region. *Nano Lett.* **12**, 3749–3755 (2012).
5. Yu, Y. F. et al. High-transmission dielectric metasurface with 2π phase control at visible wavelengths. *Laser Photonics Rev.* **9**, 412–418 (2015).
6. Shalaev, M. I. et al. High-efficiency all-dielectric metasurfaces for ultracompact beam manipulation in transmission mode. *Nano Lett.* **15**, 6261–6266 (2015).

7. Chong, K. E. et al. Polarization-independent silicon metadevices for efficient optical wavefront control. *Nano Lett.* **15**, 5369–5374 (2015).
8. Khaidarov, E. et al. Asymmetric nanoantennas for ultrahigh angle broadband visible light bending. *Nano Lett.* **17**, 6267–6272 (2017).
9. Komar, A. et al. Dynamic beam switching by liquid crystal tunable dielectric metasurfaces. *ACS Photonics* **5**, 1742–1748 (2018).
10. Emani, N. K. et al. High-efficiency and low-loss gallium nitride dielectric metasurfaces for nanophotonics at visible wavelengths. *Appl. Phys. Lett.* **111**, 221101 (2017).
11. Lin, D., Fan, P., Hasman, E. & Brongersma, M. L. Dielectric gradient metasurface optical elements. *Science* **345**, 298–302 (2014).
12. Arbabi, A., Horie, Y., Ball, A. J., Bagheri, M. & Faraon, A. Subwavelength-thick lenses with high numerical apertures and large efficiency based on high-contrast transmitarrays. *Nat. Commun.* **6**, 7069 (2015).
13. Khorasaninejad, M. et al. Metalenses at visible wavelengths: diffraction-limited focusing and subwavelength resolution imaging. *Science* **352**, 1190–1194 (2016).
14. Paniagua-Dominguez, R. et al. A metalens with a near-unity numerical aperture. *Nano Lett.* **18**, 2124–2132 (2018).
15. Shcherbakov, M. R. et al. Enhanced third-harmonic generation in silicon nanoparticles driven by magnetic response. *Nano Lett.* **14**, 6488–6492 (2014).
16. Liu, S. et al. Resonantly enhanced second-harmonic generation using III−V semiconductor all-dielectric metasurfaces. *Nano Lett.* **16**, 5426–5432 (2016).
17. Camacho-Morales, R. et al. Nonlinear generation of vector beams from AlGaAs nanoantennas. *Nano Lett.* **16**, 7191–7197 (2016).
18. Grinblat, G., Li, Y., Nielsen, M. P., Oulton, R. F. & Maier, S. A. Enhanced third harmonic generation in single germanium nanodisks excited at the anapole mode. *Nano Lett.* **16**, 4635–4640 (2016).
19. Greffin, J. M. et al. Magnetic and electric coherence in forward- and back-scattered electromagnetic waves by a single dielectric subwavelength sphere. *Nat. Commun.* **3**, 1171 (2012).
20. Fu, Y. H., Kuznetsov, A. I., Miroshnichenko, A. E., Yu, Y. F. & Luk'yanchuk, B. Directional visible light scattering by silicon nanoparticles. *Nat. Commun.* **4**, 1527 (2013).
21. Person, S. et al. Demonstration of zero optical backscattering from single nanoparticles. *Nano Lett.* **13**, 1806–1809 (2013).
22. Zhao, W. et al. Dielectric Huygens' metasurface for high-efficiency hologram operating in transmission mode. *Sci. Rep.* **6**, 30613 (2016).
23. Chong, K. E. et al. Efficient polarization-insensitive complex wavefront control using Huygens' metasurfaces based on dielectric resonant meta-atoms. *ASC Photonics* **3**, 514–519 (2016).
24. Arbabi, A., Horie, Y., Bagheri, M. & Faraon, A. Dielectric metasurfaces for complete control of phase and polarization with subwavelength spatial resolution and high transmission. *Nat. Nanotech* **10**, 937–943 (2015).
25. Paniagua-Dominguez, R. et al. Generalized Brewster effect in dielectric metasurfaces. *Nat. Commun.* **7**, 10362 (2016).
26. Staude, I. et al. Shaping photoluminescence spectra with magnetoelectric resonances in all-dielectric nanoparticles. *ACS Photonics* **2**, 172–177 (2015).
27. Caldarola, M. et al. Non-plasmonic nanoantennas for surface enhanced spectroscopies with ultra-low heat conversion. *Nat. Commun.* **6**, 7915 (2015).
28. Regmi, R. et al. All-dielectric silicon nanogap antennas to enhance the fluorescence of single molecules. *Nano Lett.* **16**, 5143–5151 (2016).
29. Dmitriev, P. A. et al. Resonant Raman scattering from silicon nanoparticles enhanced by magnetic response. *Nanoscale* **8**, 9721–9726 (2016).
30. Totero Gongora, J. S., Miroshnichenko, A. E., Kivshar, Y. S. & Fratalocchi, A. Anapole nanolasers for mode-locking and ultrafast pulse generation. *Nat. Commun.* **8**, 15535 (2017).
31. Plotnik, Y. et al. Experimental observation of optical bound states in the continuum. *Phys. Rev. Lett.* **107**, 183901 (2011).
32. Hsu, C. W. et al. Observation of trapped light within the radiation continuum. *Nature* **499**, 188–191 (2013).
33. Hsu, C. W., Zhen, B., Stone, A. D., Joannopoulos, J. D. & Soljacic, M. Bound states in the continuum. *Nat. Rev. Mater.* **1**, 16048 (2016).
34. Bulgakov, E. N. & Maksimov, D. N. Light enhancement by quasi-bound states in the continuum in dielectric arrays. *Opt. Express* **25**, 14134–14147 (2017).
35. Rivera, N. et al. Controlling directionality and dimensionality of radiation by perturbing separable bound states in the continuum. *Sci. Rep.* **6**, 33394 (2016).
36. Rybin, M. V. et al. High-Q supercavity modes in subwavelength dielectric resonators. *Phys. Rev. Lett.* **119**, 243901 (2017).
37. Sadrieva, Z. F. et al. Transition from optical bound states in the continuum to leaky resonances: role of substrate and roughness. *ACS Photonics* **4**, 723–727 (2017).
38. Han, S. et al. All-dielectric active photonics driven by bound states in the continuum. Preprint at https://arxiv.org/abs/1803.01992 (2018).
39. Imada, M. et al. Coherent two-dimensional lasing action in surface-emitting laser with triangular-lattice photonic crystal structure. *App. Phys. Lett.* **75**, 316–318 (1999).
40. Noda, S., Yokoyama, M., Imada, M., Chutinan, A. & Mochizuki, M. Polarization mode control of two-dimensional photonic crystal laser by unit cell structure design. *Science* **293**, 1123–1125 (2001).
41. Hirose, K. et al. Watt-class high-power, high-beam-quality photonic-crystal lasers. *Nat. Photon* **8**, 406–411 (2014).
42. Kodigala, A. et al. Lasing action from photonic bound states in continuum. *Nature* **541**, 196–199 (2017).
43. Miyai, E. et al. Photonics: lasers producing tailored beams. *Nature* **441**, 946 (2006).
44. Zhen, B., Hsu, C. W., Lu, L., Stone, A. D. & Soljacic, M. Topological nature of optical bound states in the continuum. *Phys. Rev. Lett.* **113**, 257401 (2014).
45. Sze, S. M. & Ng, K. K. *Physics of Semiconductor Devices* 3rd edn (Wiley, New York, 2007).
46. Palik, E. D. *Handbook of Optical Constants of Solids* (Elsevier, San Diego, 1997).
47. Liu, S., Keeler, G. A., Reno, J. L., Sinclair, M. B. & Brener, I. III−V semiconductor nanoresonators—a new strategy for passive, active, and nonlinear all-dielectric metamaterials. *Adv. Opt. Mater.* **4**, 1457–1462 (2016).
48. Löchner, F. et al. Polarization-dependent second harmonic diffraction from resonant GaAs metasurfaces. *ACS Photonics* **5**, 1786–1793 (2018).
49. Chang, C. C. et al. Electrical and optical characterization of surface passivation in GaAs nanowires. *Nano Lett.* **12**, 4484–4489 (2012).
50. Chow, W. W., Jahnke, F. & Gies, C. Emission properties of nanolasers during the transition to lasing. *Light Sci. Appl.* **3**, e201 (2014).
51. Pan, S. H., Gu, Q., Amili, A. E., Vallini, F. & Fainman, Y. Dynamic hysteresis in a coherent high-β nanolaser. *Optica* **3**, 1260–1265 (2016).
52. Taghizadeh, A. & Chung, I.-S. Quasi bound states in the continuum with few unit cells of photonic crystal slab. *Appl. Phys. Lett.* **111**, 031114 (2017).

Acknowledgements

Author contributions

S.T.H. and Y.H.F. constructed the low-temperature emission measurement set-up and performed the optical characterization. S.T.H. performed the photon autocorrelation measurements and wrote the first draft of the manuscript. N.K.E. optimized the fabrication process, prepared the samples and performed initial-stage optical characterization and analyses. Z.P. assisted in constructing the low-temperature emission measurement set-up. R.M.B. helped with the initial stage of the optical measurements. R.P.-D. conceived the idea of a BIC laser in the nanoantenna arrays, and performed the simulations. A.I.K. conceived the idea of resonant semiconductor nanoantenna lasers and supervised the work. All authors discussed the results and worked on the manuscript.

Competing interests

The authors declare no competing interests.

Additional information

Supplementary information is available for this paper at https://doi.org/10.1038/s41565-018-0245-5.

Reprints and permissions information is available at www.nature.com/reprints.

Correspondence and requests for materials should be addressed to A.I.K.

Publisher's note: Springer Nature remains neutral with regard to jurisdictional claims in published maps and institutional affiliations.

Methods

Back focal plane spectroscopy. The measurements were performed with an inverted optical microscope set-up (Nikon Ti-U) coupled to a spectrometer (Andor SR-303i) equipped with an EMCCD detector (Andor Newton)[3]. Light from a halogen lamp polarized along the x axis was focused on the sample surface via a top objective (×50, 0.55 NA). The transmission signal was then collected by a lower objective with the same specifications. The back focal plane of the bottom objective was imaged onto the entrance slit of the spectrometer. The slit had a width of 50 μm and was oriented along the x axis of the sample. This measurement provided an angular-resolved transmission spectrum of the sample in a single image (see Fig. 2b). Angular information was recorded along the slit axis of the spectrometer (that is, corresponding to a variation of the angle of incidence contained in the x–z plane of the sample). The maximum detected angle was determined by the NA of the objective and was ~33° for the lens used.

Numerical simulations. Numerical simulations presented in the paper were performed using a commercial solver based on the finite element method (COMSOL Multiphysics). The simulation domain consisted of a rectangular box, representing a unit cell of the array, and a cylinder representing the GaAs nanopillar. Periodic Bloch boundary conditions were applied in the boundaries along the x and y directions to mimic an infinite, 2D system. The periodicities of the array were $P_x = 300$ nm and $P_y = 540$ nm (corresponding to the physical size of the rectangular box in the x and y directions, respectively). Port boundary conditions were used in the top and bottom boundaries to excite the system and to collect outgoing waves, both in transmission and reflection. As many ports as diffraction orders supported by the lattice were used both in transmission and reflection. The excitation field corresponded to that of a p-polarized plane wave incident onto the array at a certain angle, θ, contained in the x–z plane. The total size of the rectangular box was 1 μm in the z direction. GaAs particles were modelled as cylinders with height $H = 250$ nm and diameter $D = 100$ nm, and were considered to be embedded in a background material with a refractive index of 1.45. The material parameters used for GaAs were those experimentally measured by ellipsometry in the GaAs films used. In the transmission results presented in Fig. 2d, only the direct transmission is plotted.

The multipole decomposition presented in Fig. 2e is based on the decomposition of the particle internal fields using a Cartesian basis. The electric dipole moment excited in the particle can be calculated as:

$$\mathbf{p} = \int \varepsilon_0 (\varepsilon - \varepsilon_d) \mathbf{E} d\mathbf{r} \tag{1}$$

In this expression, ε_0 is the permittivity of vacuum, ε_d and ε are the relative permittivities of the surrounding medium and the particle, respectively, $\mathbf{E} = \mathbf{E}(\mathbf{r})$ is the vector electric field and the integral is taken over the volume of the particle. From this calculation, one can readily identify the main component of the electric dipole induced in the particles, as done in Fig. 2e, in which both horizontal and vertical induced electric dipoles could be identified. From the dipole moments, it is then possible to compute the scattering cross-section associated with them as:

$$C_{\mathrm{ED}} = \frac{k_0^4}{6\pi\varepsilon_0^2 E_0^2} |\mathbf{p}|^2 \tag{2}$$

The rest of the multipole moments (not shown in this paper) can also be computed from the internal fields of the particle following expressions detailed elsewhere[25].